Science Advances
AAAS

Supplementary Materials for

Atomically engineered cobaltite layers for robust ferromagnetism

Shengru Chen *et al.*

Corresponding author: Wen Yin, yinwen@ihep.ac.cn; Kui-juan Jin, kjjin@iphy.ac.cn; Er Jia Guo, ejguo@iphy.ac.cn

Sci. Adv. **8**, eabq3981 (2022)
DOI: 10.1126/sciadv.abq3981

This PDF file includes:

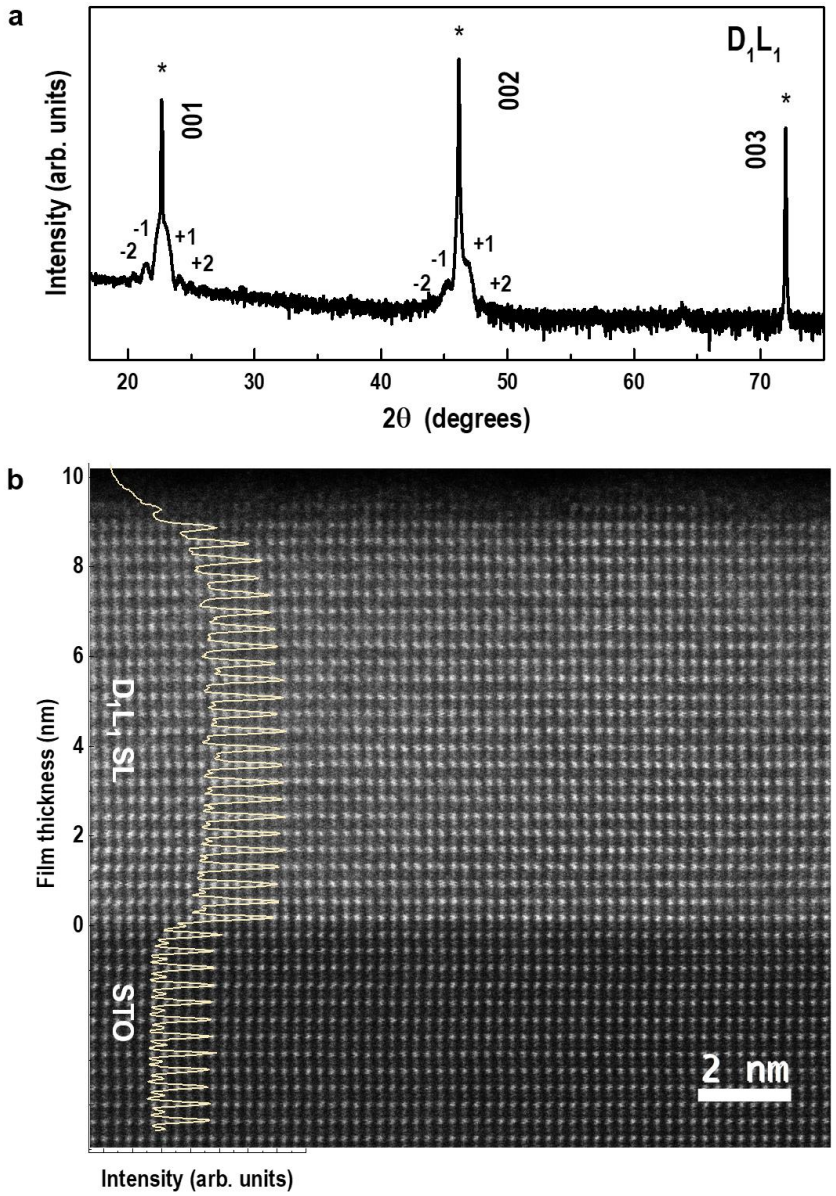

Figure S1. Structural characterizations of D_1L_1 SL. (a) XRD θ-2θ scan of D_1L_1 SL. The "*" denotes the STO substrate's 00*l* reflections. The 00*l* reflections from D_1L_1 SL are overlapped with substrate's reflections. The clear Kiessig fringes around film's peaks suggest that SL is epitaxially grown with extremely high quality. (b) Cross-sectional HAADF STEM image of D_1L_1 SL. The sample was imaged along the pseudocubic [110] zone axis. Inset shows the HAADF intensity as a function of film thickness. The heavier elements (Sr, La, Dy) with the larger atomic number show brighter features in HAADF image. From STEM image and depth profile, we find the distinct interfaces between SLs and STO substrates are atomically sharp. Please note that the atomic numbers between Sc and Co as well as between Dy and La are very close to each other. We could not identify the elements from the intensities in HAADF image.

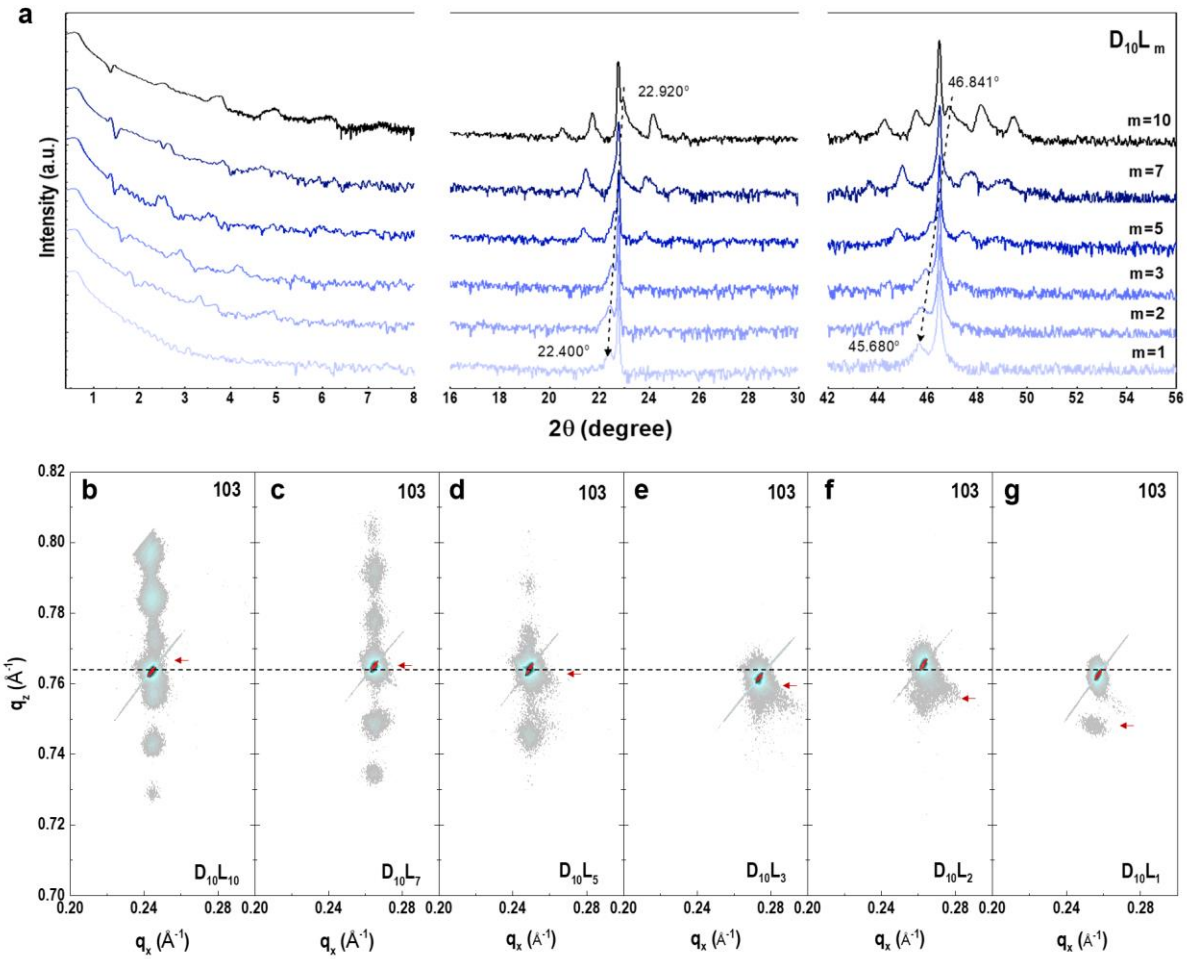

Figure S2. Structural characterizations of $D_{10}L_m$ SLs. (a) XRD θ-2θ scans and (b) Reciprocal space mappings (RSMs) around the substrate's 103 reflections of $D_{10}L_m$ SLs for m =1, 2, 3, 5, 7, 10, where m represents the number of LCO's unit cell (u. c.). As increasing m, the SL peak shifts towards the large angles, suggesting the averaged out-of-plane lattice constant of SL reduces. The Kiessig fringes around the SL's main peaks and Bragg peaks indicate that all SLs are highly epitaxially grown and have the high crystalline quality. RSM results suggest all SLs are coherently strained by substrates. Red arrows indicate that the peak positions of SLs gradually shift to smaller q_z, indicating the increment of lattice constant.

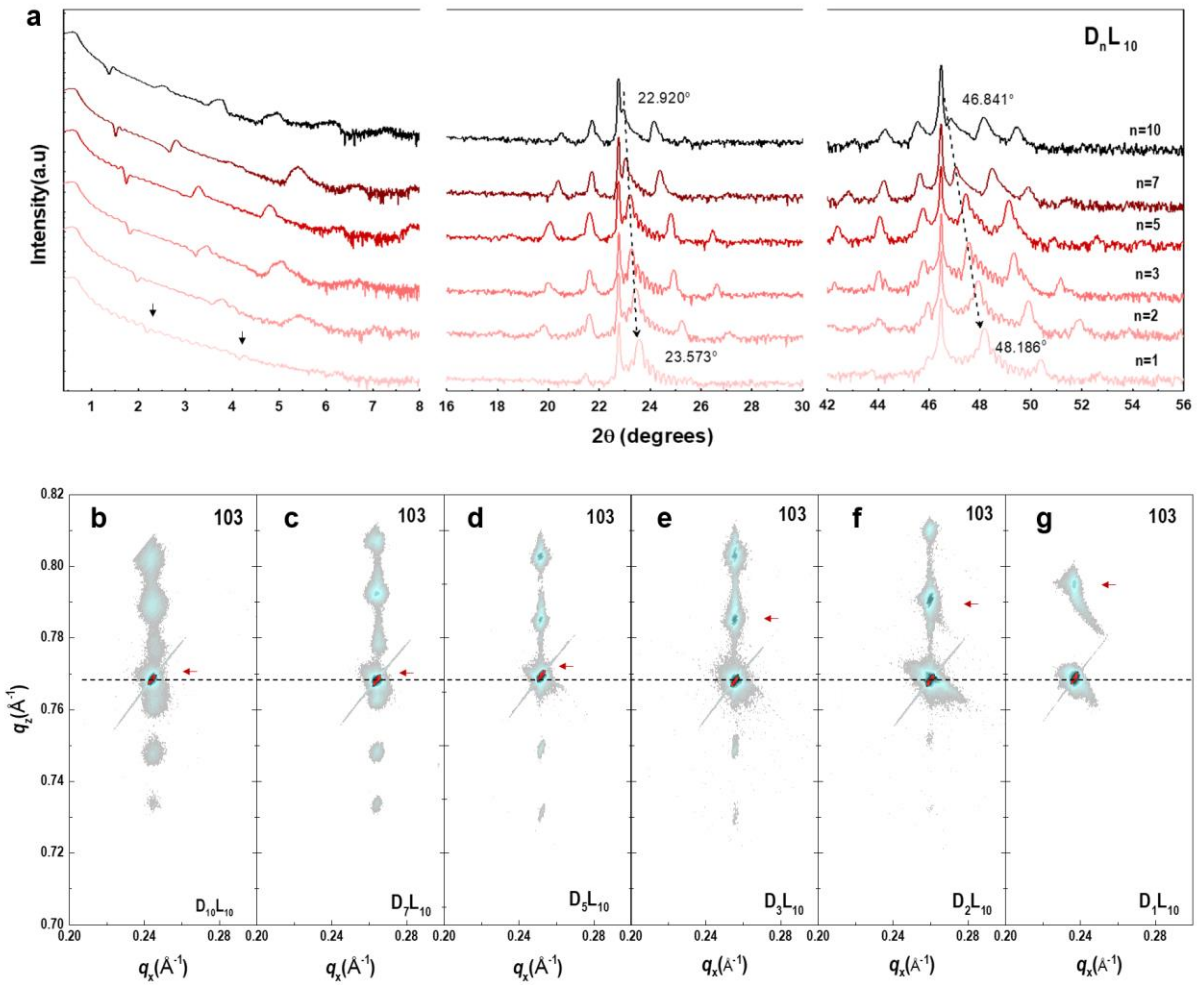

Figure S3. Structural characterizations of D_nL_{10} SLs. (a) XRD θ-2θ scans and (b) RSMs around substrate's 103 reflections of D_nL_{10} SLs for n =1, 2, 3, 5, 7, 10, where n represents the number of DSO's u. c.. With increasing DSO layer thickness, the SL peaks move to low angles, indicating the averaged out-of-plane lattice constant of SL increases. We observe up to 3 orders of SL Bragg peaks and thickness fringes around SL main peaks, suggesting that all SLs have high crystallinity. Similar to Figure S2, RSM results suggest all SLs are coherently strained by substrates.

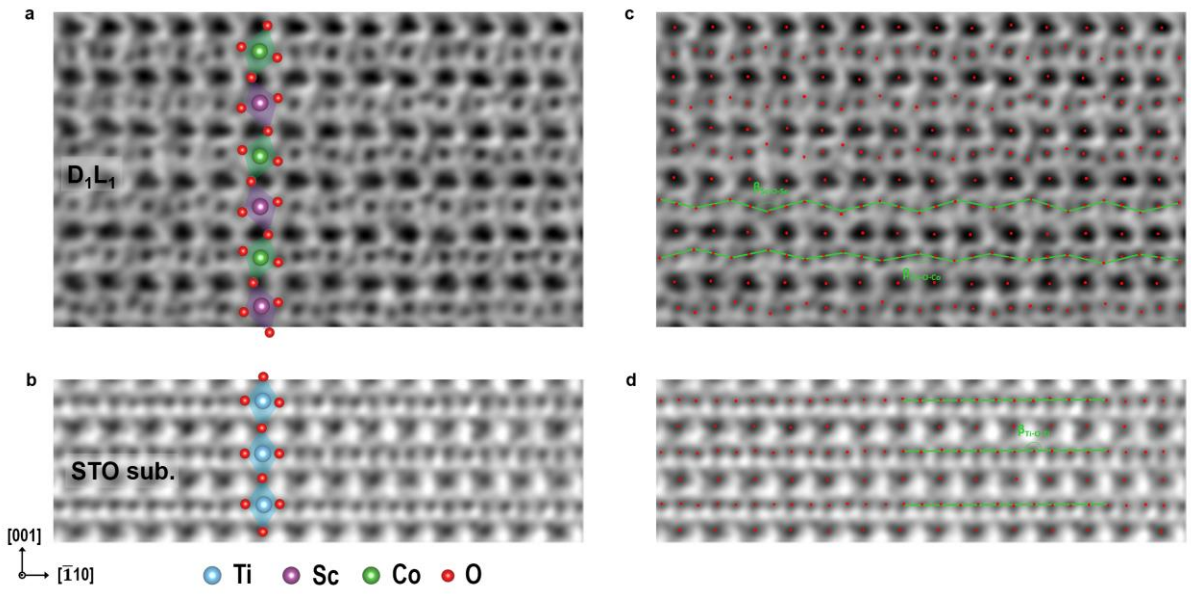

Figure S4. **Estimation of bonding angles in D_1L_1 SL.** (a) and (b) ABF-STEM images of film region and substrate region in D_1L_1 SL, respectively. The schematics of oxygen octahedral tilts for ScO_6, CoO_6, and TiO_6 are illustrated. (c) and (d) The ABF-STEM images from the same area that used for analyzing the bonding angles. Small red dots represent the atomic columns positions of each atom that determined by fitting the intensity peaks with Gaussian function. The parameters of this model, including the atomic column position, the height and width of the Gaussian peak, have been calculated using the least squares estimator. From these positions, the B-O-B (B = Sc, Co, and Ti) bonding angles can be determined by measuring the angle between two straight lines crossing pairs of neighboring light O atoms. The $\beta_{\text{B-O-B}}$ is averaged over at least thirty pairs of B-O-B bonding angles within each layer. With this method, the layer position dependent mean values of $\beta_{\text{B-O-B}}$ together with their standard deviations have been determined. The results are shown in Figure 1b of main text.

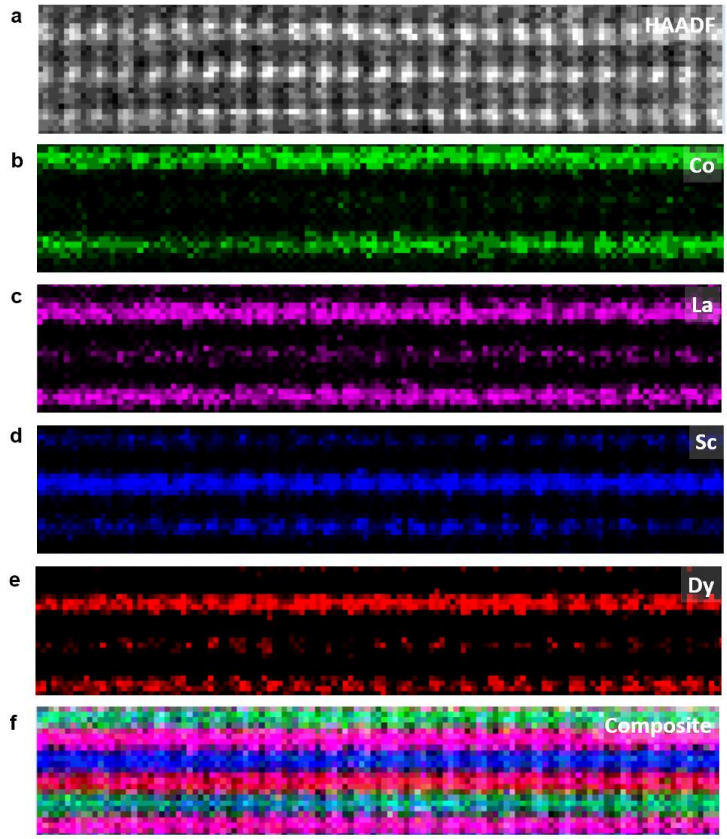

Figure S5. Atomically resolved STEM-EDX mapping of D_1L_1 SL. (a) HAADF image of interested region. (b)-(e) Element-selective EDX results on Co, La, Sc, and Dy, respectively. We find that the Co and Sc, which locate at the center positions of octahedra, separate clearly with minimal chemical intermixing. The composite overlaid EDX image, as shown in (f), demonstrates the nicely separation of each element over three-unit-cells of D_1L_1 SL.

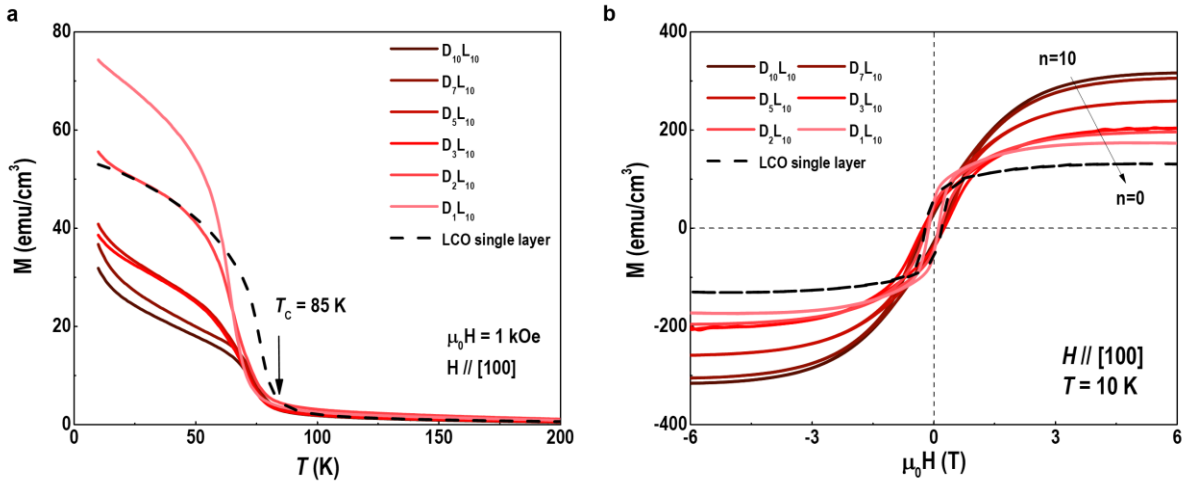

Figure S6. Magnetization characterizations of D_nL_{10} SLs. (a) *M-T* curves of D_nL_{10} SLs for $1 \leq n \leq 10$. The *M-T* curves were measured under a magnetic field of 1 kOe applied along the [100] orientation after field-cooling. *M-T* results show that LCO single layer and all SLs exhibit clear paramagnetic-ferromagnetic phase transitions. T_C of LCO single layer is ~ 85 K, whereas T_C of SLs decreases to 75 ± 3 K. The reduction of T_C is attributed to the finite size effect. (b) *M-H* loops of D_nL_{10} SLs. *M-H* loops were recorded at 10 K under in-plane magnetic field in parallel to [100] orientation. All samples exhibit clear hysteresis loops, indicating the ferromagnetic character at low temperatures. As increasing DSO layer's thickness, the saturation moment increases due to the paramagnetic contribution from DSO layers.

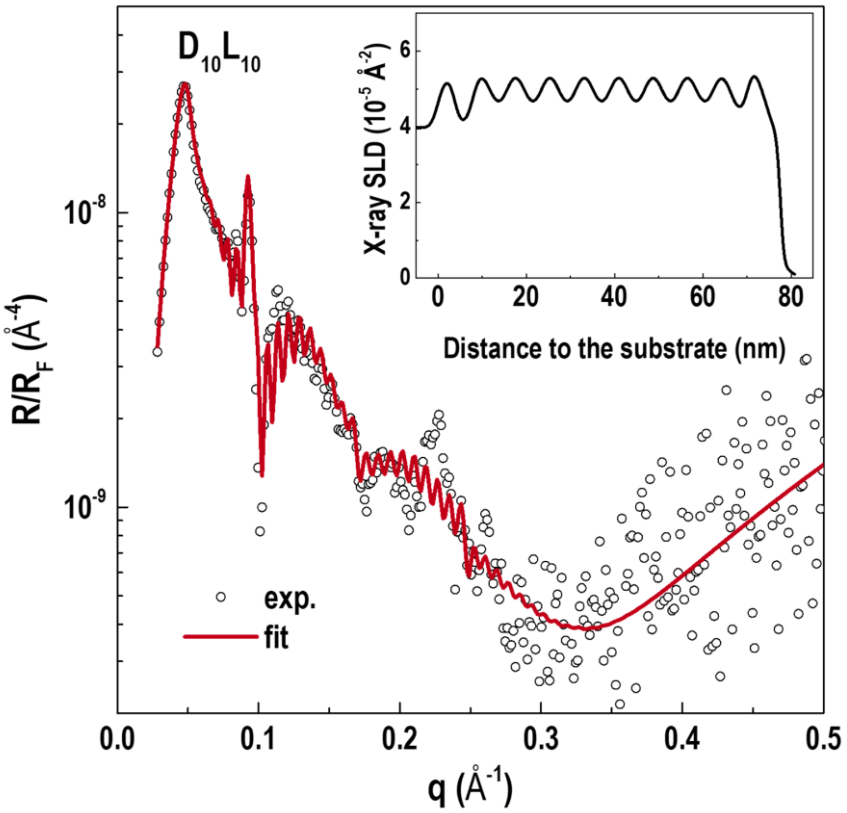

Figure S7. XRR of $D_{10}L_{10}$ SL. The solid line is the best fit to the experimental data (open symbols). The thicknesses of DSO and LCO layers are 39.2 ± 4.6 Å and 38.5 ± 3.9 Å, respectively. The DSO/LCO bilayer repeats 10 times. The total thickness of $D_{10}L_{10}$ SL is 79.8 ± 0.9 nm. Inset shows the X-ray scattering length density (SLD) profile of $D_{10}L_{10}$ SL. The X-ray SLD of LCO layer (~5.2×10^{-5} Å^{-2}) is larger than that of DSO layer (~ 4.5×10^{-5} Å^{-2}). The chemical composition of SL is used to constrain the chemical depth profile for PNR fittings in Figs. 2d-2f. We use the GenX software to fit XRR and PNR curves.

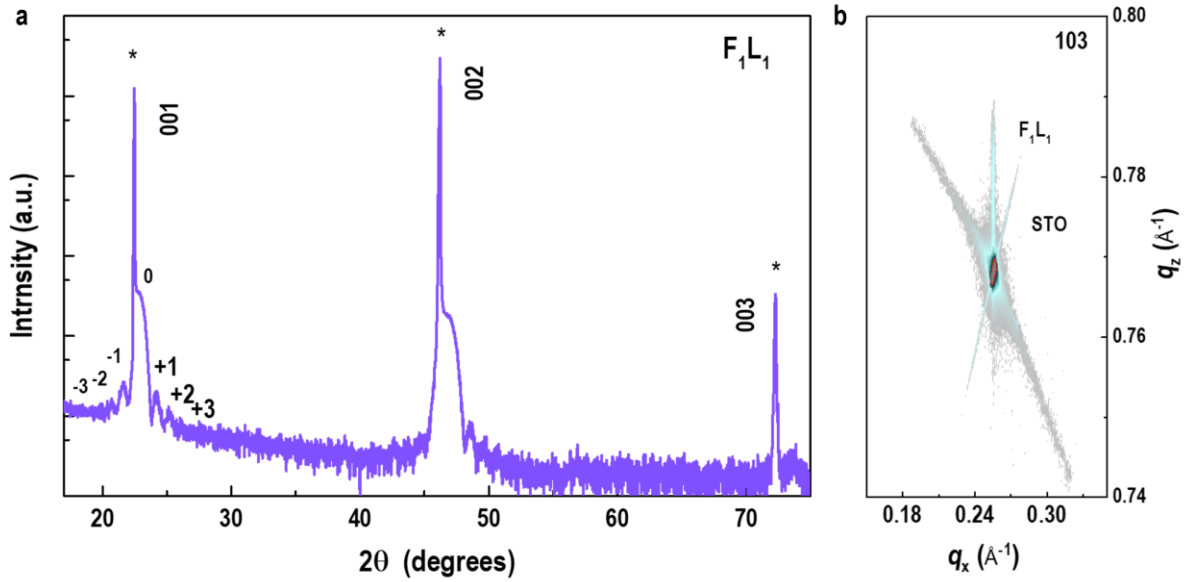

Figure S8. **Structural characterizations of F_1L_1 SL**. (a) XRD θ-2θ scan of F_1L_1 SL. The "*" denotes the STO substrate's 00*l* reflections. The lattice constant of LFO is smaller than that of DSO, thus the averaged lattice constant of F_1L_1 SL is smaller than that of D_1L_1 SL. We observe the main peak of SL shifts to the right side of the substrate's reflections. Similar to Figure S1, the clear Kiessig fringes around the 001 and 002 peaks persist up to the 3rd order, indicating that SL is epitaxially grown with extremely high crystalline quality. (b) RSM around substrate's 103 reflections of F_1L_1 SL, suggesting all layers are coherently strained to STO substrates.

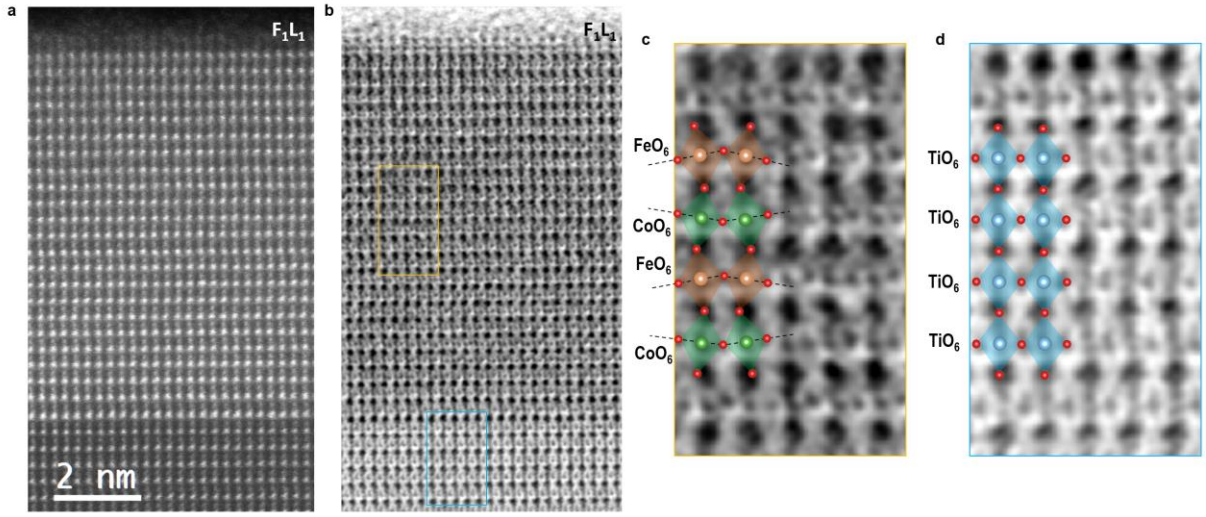

Figure S9. STEM results of F_1L_1 SL. Cross-sectional (a) HAADF-STEM and (b) ABF-STEM images of a F_1L_1 SL. The number of atomic layers is clearly visualized to confirm the designed structure. The interfaces between SL and STO substrates are proven to be atomically sharp. STEM results manifest itself a coherent and alternative LFO-LCO layers with a fully-strained state. The large tensile strain up to ~2.5% is applied to LCO layers. Zoom-in ABF images marked in orange and blue rectangles in (b) represent SL layers and STO substrates, as shown in (c) and (d), respectively. In contrast to untilted TiO_6 octahedra in STO substrates, the CoO_6 octahedra follow the tilt patterns of FeO_6 octahedra. We could identify the octahedral tilt angle is ~15° ± 3°, corresponding to $\beta_{Co\text{-}O\text{-}Co}$ ~150° ± 5°. This feature is similar to the octahedral tilt in D_1L_1 SL, as shown in Figure 1. STEM results highlight the importance of octahedral tilting in controlling the spin states of transition metal ions.

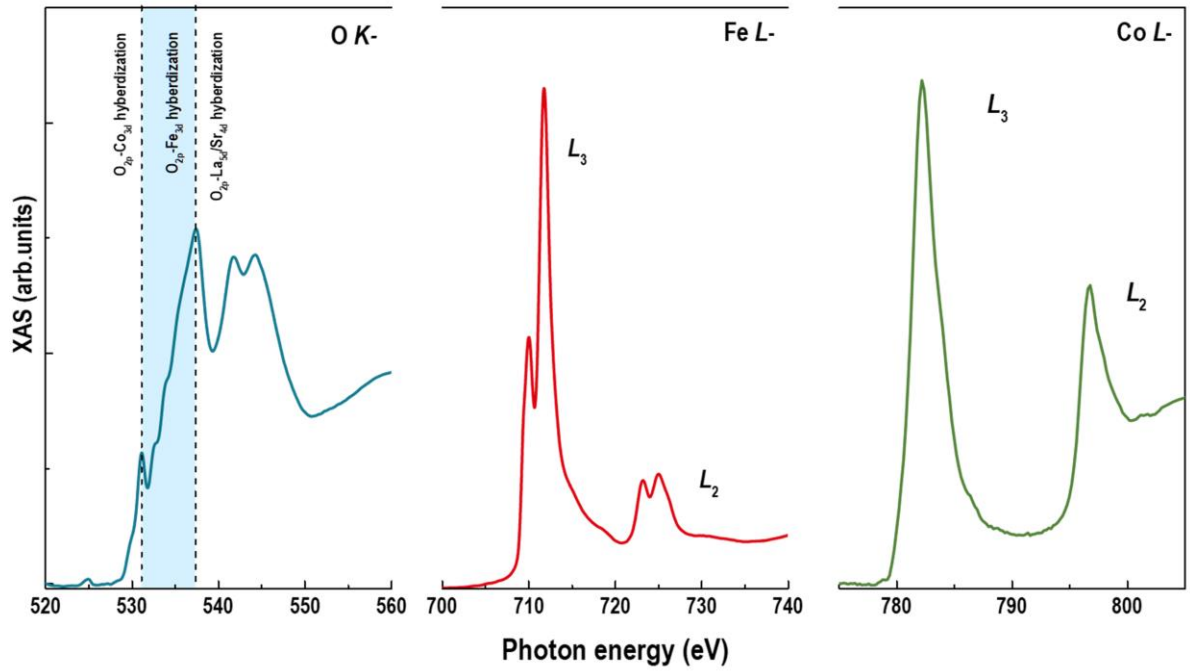

Figure S10. XAS measurements of F_1L_1 SL. XAS at O *K*-, Fe *L*-, and Co *L*-edges were measured at room temperature. XAS results indicate that Fe ions and Co ions keep +3, indicating the negligible charge transfer between Co and Fe ions. This fact is important for analyzing the spin states of Co ions within F_1L_1 SL.

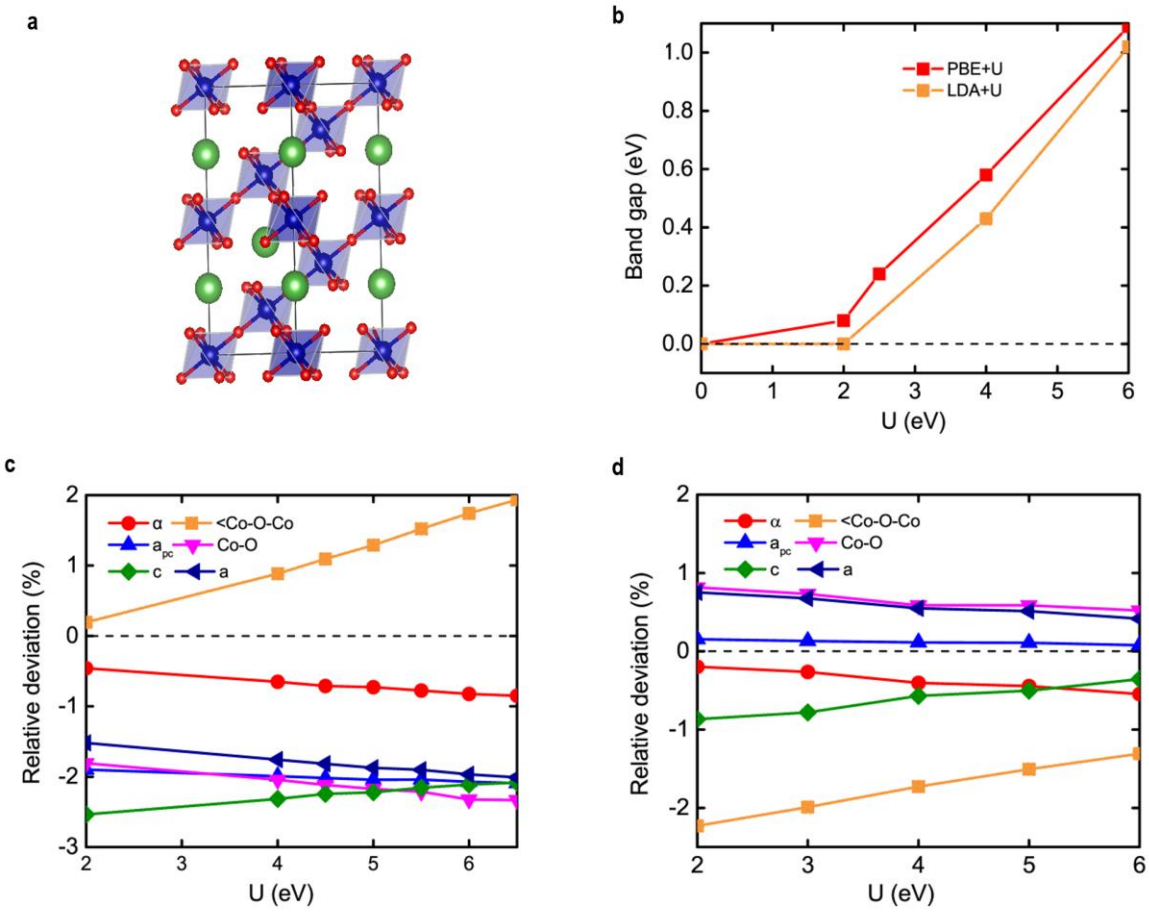

Figure S11. Structural parameters and calculation details. (a) The crystal structure of bulk LCO. (b) Band gaps of the optimized low spin state LCO using LSDA+U and sPBE+U method. (c) and (d) Lattice constants (*a,c*), pseudo-cubic constants (a_{pc}), Co-O-Co bond lengths, rhombohedral tilting angles (α), and Co-O-Co bond angles for the optimized low spin state LCO using LDA+U and PBE+U methods, respectively. Both methods exhibit similar trends, verifying the intrinsic property of LCO with different on-site Coulomb interactions.

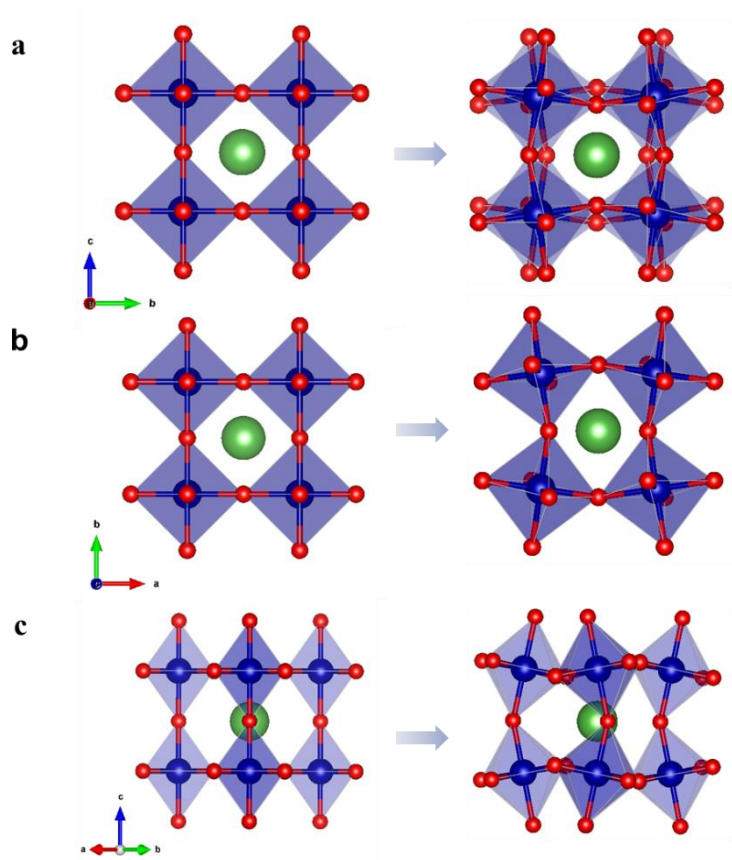

Figure S12. Crystal structures with different tilting patterns. (a), (b), and (c) Schematic crystal structures of 2 × 2 × 2 supercells along the pseudocubic [100], [001], and [110] zone axis, respectively. The supercells are without (lefthand) and with (righthand) octahedral tilt, corresponding to the $a^0a^0a^0$ non-tilted pattern (S_1L_1 SL) and $a^-a^-c^+$ tilt pattern (D_1S_1 and F_1L_1 SLs), respectively.

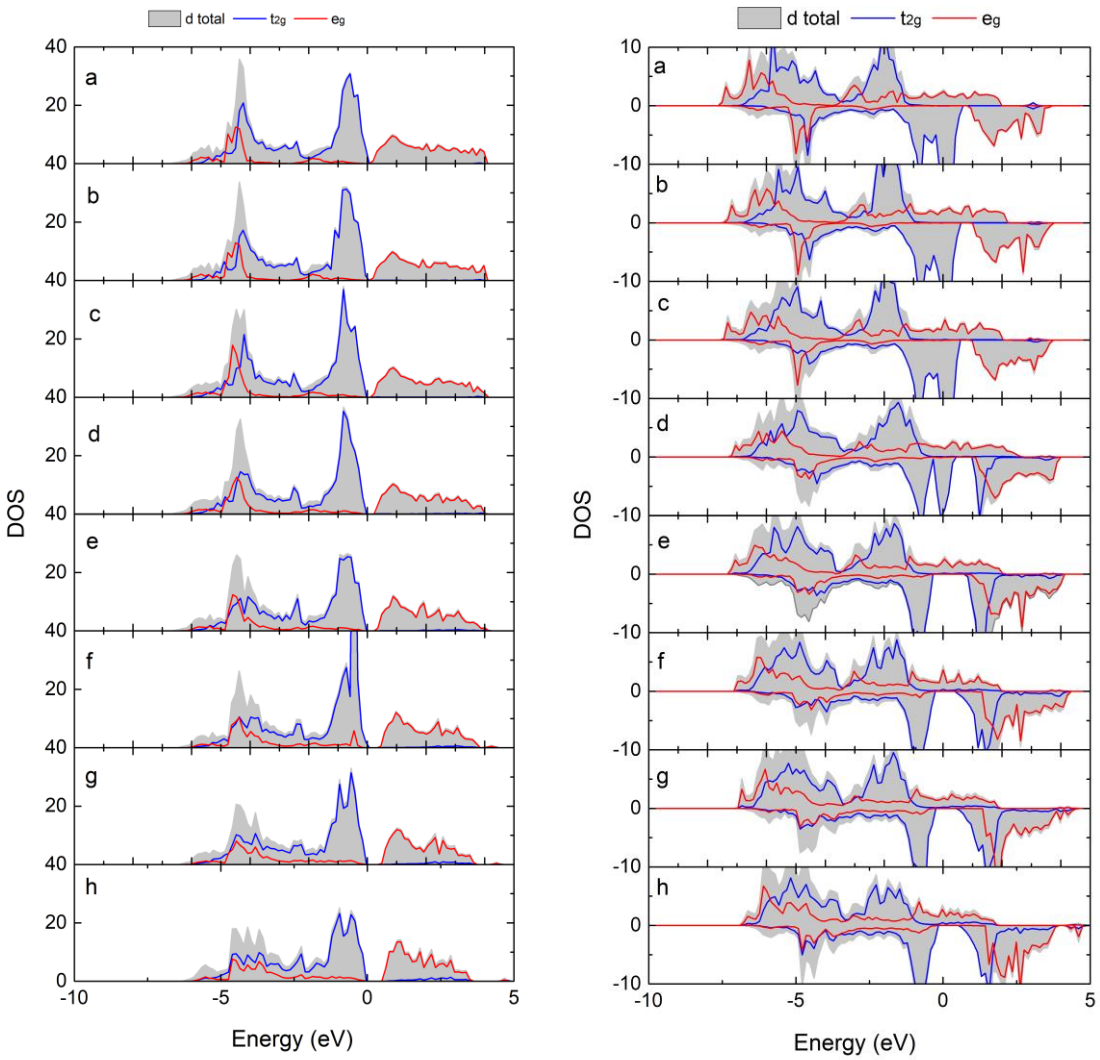

Figure S13. Projected density of states (DOS) for LS (lefthand) and IS (righthand) states $LaCoO_3$ with rotation amplitude varying from 0% to 7%. The gray area, bule lines, and red lines represent the Co ions *d* total, t_{2g} and e_g, respectively.

Table S1. Structural parameters for an initial LCO with a rotation pattern between $a^-a^-a^-$ and $a^0a^0a^0$. The lattice parameters were optimized using DFT calculations. Both tilted and non-tilted lattice structures are considered. The in-plane lattice parameter (a) of LCO is constrained by that of STO substrates. The out-of-plane lattice parameter (c) of LCO is optimized with minimizing the free energy. $\beta_{\text{B-O-B}}$ and $\beta'_{\text{B-O-B}}$ represent the octahedral rotation angle clockwise or counter-clockwise with respect to the in-plane direction. We summarize the calculated structural parameters of LCO with LS (IS) configuration, as listed below.

	strain (%)	***a* (Å)**	***c* (Å)**	$\boldsymbol{\beta}_{\textbf{B-O-B}}$ **(°)**	$\boldsymbol{\beta'}_{\textbf{B-O-B}}$ **(°)**
Without tilting	2	3.905	3.77(3.81)	180(180)	180(180)
With tilting	2	3.905	3.78(3.85)	161.21(160.35)	155.85(159.7)